water

MDPI

Article

Fabrication of MoS_2@Fe_3O_4 Magnetic Catalysts with Photo-Fenton Reaction for Enhancing Tetracycline Degradation

Zong-Lai Liu [1], Jia-Hong Sun [2], Bing Liu [3], Ya-Nan Chen [1] and Wei Feng [2,*]

[1] College of Jilin Emergency Management, Changchun Institute of Technology, Changchun 130012, China
[2] Key Lab of Groundwater Resources and Environment, Ministry of Education, Jilin University, Changchun 130021, China
[3] College of Life and Environmental Science, Wenzhou University, Wenzhou 325035, China
* Correspondence: weifeng@jlu.edu.cn

Abstract: Tetracycline (TCs) is widely used in the treatment of human and animal infectious disease. TCs gives rise to a growing threat to the human health and environment protection due to its overuse. Therefore, it is important to remove TCs contaminants from waste effluents. In this work, MoS_2@Fe_3O_4 catalytic material was fabricated by the simple hydrothermal method, which was applied in the photo-Fenton system to degrade TCs. The crystal structure, surface morphology, elemental composition, chemical state, electrochemical properties, and separability of MoS_2@Fe_3O_4 catalytic materials were analyzed by X-ray diffraction (XRD), scanning electron microscope (SEM), conventional and high-resolution transmission electron microscopy (TEM/HRTEM), X-ray photoelectron spectroscopy (XPS), electrochemical impedance spectroscopy (EIS), and vibrating sample magnetometry (VSM). Furthermore, MoS_2@Fe_3O_4 could degrade 98.6% of TCs within 60 min under the optimum reaction conditions (the catalyst dosage of 3 g/L, H_2O_2 concentration of 5 mmol/L, the initial TCs concentration of 50 mg/L, and the initial pH of 5), which was a significant increase compared with pure Fe_3O_4. MoS_2 can accelerate the Fe^{3+}/Fe^{2+} cycle through electron transfer from Mo^{4+} to Fe^{3+}, resulting in the improvement in the degradation efficiency of TCs. The quenching and electron paramagnetic resonance (EPR) results showed that $OH^{\bullet}$ and photogenic hole h+ was the main active species in the photo-Fenton system. What is more, MoS_2@Fe_3O_4 catalytic materials had remarkable stability and reusability, and can be handily regained via magnetic separation technology in a real scenario.

Keywords: photo-Fenton; MoS_2@Fe_3O_4; magnetic separation; visible light; tetracycline

check for updates

Academic Editor: Liping Wang

Received: 9 December 2024
Revised: 14 January 2025
Accepted: 14 January 2025
Published: 16 January 2025

Citation: Liu, Z.-L.; Sun, J.-H.; Liu, B.; Chen, Y.-N.; Feng, W. Fabrication of MoS_2@Fe_3O_4 Magnetic Catalysts with Photo-Fenton Reaction for Enhancing Tetracycline Degradation. *Water* **2025**, *17*, 235. https://doi.org/10.3390/w17020235

Copyright: © 2025 by the authors. Licensee MDPI, Basel, Switzerland. This article is an open access article distributed under the terms and conditions of the Creative Commons Attribution (CC BY) license (https://creativecommons.org/licenses/by/4.0/).

1. Introduction

Compared with other antibiotics, tetracycline (TCs) is widely used in animal husbandry, aquaculture industry, and the medical industry due to its advantages of low cost, good effects, and wide antibacterial range [1,2]. Because it is biologically active, stable, and non-biodegradable, TCs has now been detected in surface water, groundwater, and sediments [3]. Residual TCs in the environment can threaten the aquatic and microbial community structure and increase the risk posed by antibiotic-resistant pathogens, which can be transferred throughout the food chain, causing longer-term harm to the environment and human health [4,5]. Therefore, how to efficiently remove TCs pollutants has gradually become a research hotspot.

Several methods, including physical adsorption [6,7], membrane treatment [8], biodegradation [9,10], advanced oxidation processes (AOPs) such as photocatalytic degradation [11], ozonation [12], Fenton and Fenton-like technology [13,14], and photo-Fenton

processes [15], are utilized to remove TCs from polluted water. Specifically, the heterogeneous photo-Fenton process, which combined the features of photocatalysis and Fenton method, can realize the rapid degradation of TCs. Due to the use of sunlight as a light source, the photocatalytic reaction process is green non-pollution and huge energy release. Meanwhile, the introduction of hydrogen peroxide (H_2O_2) can boost the yield of $OH^•$, form an iron cycle reaction, reduce the drainage of ferrous ions (Fe^{2+}), and avoid the generation of iron sludge.

In recent years, thanks to the excellent catalytic properties and magnetic characteristics, transition elements hybrid oxides have become promising catalysts in oxidative degradation. Some studies have suggested that Fe_3O_4 nanoparticles can effectively catalyze the decomposition of H_2O_2 to produce $OH^•$, and their pH range is wide, playing a leading role in the Fenton reaction. Meanwhile, Fe_3O_4 nanoparticles after reaction can be quickly separated using its magnetic properties, which reduced the formation of iron sludge [16–18]. Due to the inverse spinel structure of Fe_3O_4, electrons can transmit between Fe^{2+} and Fe^{3+} at the octahedral location, promoting the mineralization of pollutants. However, after several reaction cycles, its catalytic activity gradually decreased, and due to the rapid recombination of photoelectron hole pairs, its photocatalytic performance was not ideal, so it is necessary to modify it to enhance their catalytic activity and increase the separation rate of photo generated electron hole pairs [16,19].

MoS_2 is a typical transition-metal dichalcogenide (TMD) which features a 2D layered structure similar to that of graphene, with high edge molecular activity and an adjustable band gap [20]. MoS_2 can be transformed from an indirect band gap semiconductor to a direct band gap semiconductor as the number of layers decreases. Correspondingly, the band gap increases from 1.29 eV to 1.97 eV, extending the absorption spectrum to the visible region [21]. At the same time, MoS_2 with small sizes or fewer layers has excellent peroxidase-like activity, through which H_2O_2 can be efficaciously converted to $OH^•$ [22,23]. Therefore, MoS_2 exhibits amazing catalytic activity, excellent optical absorption, and high photothermal efficiency. Recent evidence demonstrated that MoS_2 can accelerate the Fe^{3+}/Fe^{2+} cycle through electron transfer from Mo^{4+} to Fe^{3+}, which was attributed that the standard redox potential of Mo^{4+} (E_0 = 0.65 V) being lower than that of Fe^{3+} (E_0 = 0.77 V) [24,25]. Therefore, the combination of Fe_3O_4 nanoparticles and MoS_2 enhances the H_2O_2 activation, and facilitates the Fe^{3+}/Fe^{2+} rapid cycle by MoS_2.

In this study, a series of magnetic MoS_2 @Fe_3O_4 catalysts was fabricated by a simple hydrothermal process, and its catalytic performance was explored through photo-Fenton experiments used TCs as the target pollutant. The morphology, structure, chemical composition, and electrochemical properties of the catalysts were determined using XRD, SEM, TEM, XPS, EIS, and VSM. The effects of catalyst dosage, H_2O_2 concentration, TCs initial concentration, and pH on the TCs degradation performance were studied. The stability and reusability of MoS_2 @Fe_3O_4 catalysts were verified by repeatability experiments and magnetic recovery experiments. The possible degradation mechanism was also discussed.

2. Materials and Methods

2.1. Materials and Reagents

Analytical-grade $FeSO_4·7H_2O$, $Na_2S_2O_3·5H_2O$, H_2O_2, and NaOH were purchased from Sinopharm Chemical Reagents Co., Ltd. (Shanghai, China). Tetracycline hydrochloride (TCs, analytical reagent) was obtained from Rhawn Technology Development Co., Ltd. (Shanghai, China). Ammonium molybdate ($H_8MoN_2O_4$, analytical reagent) and L-cysteine ($C_3H_7NO_2S$, analytical reagent) were obtained from Tianjin Damao Chemical reagent Factory (Tianjin, China).

2.2. Catalyst Synthesis

Fe_3O_4 powder was fabricated by the hydrothermal method [26]. They were synthesized as follows: $FeSO_4 \cdot 7H_2O$ (2.78 g) and $Na_2S_2O_3 \cdot 5H_2O$ (2.48 g) were dissolved in 50 mL distilled water to form solution A. Then, 0.8 g of NaOH were dissolved in 10 mL distilled water to form solution B. Solution A and B were mixed and evenly stirred for 20–30 min. Subsequently, the mixture was added into 100 mL Teflon-lined autoclave chamber and hydrothermally treated at 140 °C for 12 h. After cooling to room temperature, the solid was separated from the mixture by centrifugal separation, then washed three times with distilled water and anhydrous ethanol, and dried in an oven at 60 °C for 12 h. The final product was crushed to obtain the Fe_3O_4 powder.

In the synthetic process of $MoS_2@Fe_3O_4$, ammonium molybdate (0.5 g) were dissolved in 70 mL distilled water, then L-cysteine (1.4 g) was added and stirred evenly for 20 min. A certain amount of Fe_3O_4 powder was immersed in the previous solution. After ultrasonic dispersion, the solution was filled into a 100 mL hydrothermal reactor and treated at 200 °C for 24 h. Afterward, the solid was centrifuged at 10,000 rpm and rinsed repeatedly in ethanol. Subsequently, the product was dried under the vacuum condition at 60 °C. According to the mass ratio of MoS_2 and Fe_3O_4 (2%, 4%, and 6%) in the $MoS_2@Fe_3O_4$, the samples were denoted as 2% $MoS_2@Fe_3O_4$, 4% $MoS_2@Fe_3O_4$, and 6%$MoS_2@Fe_3O_4$.

2.3. Characterization Method

The physical phase and crystal structure of the sample were characterized by D8-FOCUS X-ray diffraction (XRD) in the scanning range of 5° to 70° at 2°/min using Cu-Ka as the radiation source (Bruker, Bremen, Germany). Apreo 2C scanning electron microscopy (SEM) (Thermo Fisher Scientific, Shanghai, China) was used to observe the apparent morphology of the samples, as well as to conduct EDS (EDS XD-3) (Shimadzu, Shanghai, China) analyses. The microstructure of the material was characterized by transmission electron microscopy (TEM) (JEOL, Tokyo, Japan), and the lattice of the material was characterized by HRTEM with SEAD. The elemental and chemical valence states of the materials was characterized by ESCALAB 250 X-ray photoelectron spectrometer (XPS) with Al-Kα radiation (Thermo Fisher Scientific, Shanghai, China). The Mott–Schottky test was performed by the CHI760E electrochemical workstation (Austin, TX, USA). The magnetic strength of the material in a magnetic field of 10,000 Oe was analyzed by a magnetometer (Westerville, OH, USA).

2.4. Degradation Performance Evaluation

The photo-Fenton degradation experiment was conducted with 50 mg/L TCs as the target pollutant, and a 400 W xenon lamp bulb with cut-off filters for λ = 420 nm as the light source. A certain amount of catalyst was added to 200 mL of the TCs solution, and then a certain concentration of H_2O_2 was added to the solution; then, the light source was turned on to trigger the photo-Fenton reaction. Subsequently, 4.0 mL suspension was collected every 10 min and filtered through a 0.45 μm filter. Finally, the concentration of TCs was measured using a UV spectrophotometer at 357 nm. The reusability and comparative study of $MoS_2@Fe_3O_4$ were further examined under the same conditions for five runs.

3. Results

3.1. Characterization

The crystal structure and phase composition of the prepared samples were analyzed by XRD, which are shown in Figure 1. The diffraction peaks at 30.3°, 35.6°, 43.4°, 57.4°, and 63.0° for the pure phase Fe_3O_4 sample corresponded to the characteristic peaks of the (220), (311), (400), (422), (511), and (440) crystal planes of the cubic crystal system

(equiaxial crystal system) magnetite Fe_3O_4 (JCPDS card 19-0629), respectively [27]. The characteristic diffraction peaks of each crystal plane of Fe_3O_4 can be clearly seen in the MoS_2@Fe_3O_4 samples synthesized with different mass ratios of MoS_2 and Fe_3O_4. The diffraction peak of Fe_3O_4 showed a gradually weakening trend with the increase in the MoS_2 mass, indicating that the introduction of MoS_2 did not affect the crystal plane structure of Fe_3O_4. The characteristic diffraction peak of MoS_2 was not recognized in the XRD patterns, implying that MoS_2 was amorphous in the sample. As shown in JCPDS card 37-1492, the diffraction peaks of pure MoS_2 at $2\theta_{(002)}$ = 14.39, $2\theta_{(004)}$ = 29.03, $2\theta_{(100)}$ = 32.69, $2\theta_{(101)}$ = 33.52, $2\theta_{(102)}$ = 35.87, $2\theta_{(103)}$ = 39.55, $2\theta_{(006)}$ = 44.16, $2\theta_{(105)}$ = 49.80, $2\theta_{(106)}$ = 55.98, $2\theta_{(110)}$ = 58.34, $2\theta_{(114)}$ = 64.14, $2\theta_{(108)}$ = 70.16, $2\theta_{(203)}$ = 72.79, and $2\theta_{(116)}$ = 75.99 corresponded to hexagonal structure having space group $P6_3/mmc$ [28]. The peak intensity of MoS_2 phase is noticeably weak or absent in 2% MoS_2@Fe_3O_4; however, in case of 4% MoS_2@Fe_3O_4, the intensity of the XRD characteristic peaks of MoS_2 has been improved. In fact, the main peaks of MoS_2 corresponding to planes (100), (102), and (114) are clearly visible in 4% MoS_2@Fe_3O_4, which confirmed the MoS_2 phase was introduced into the Fe_3O_4 phase.

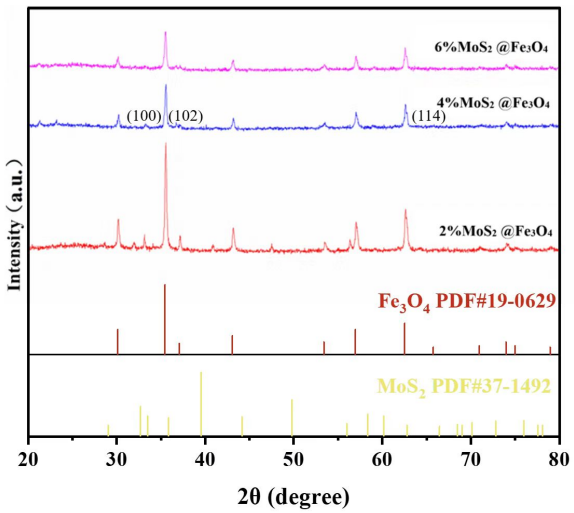


Figure 1. XRD pattern of MoS_2@Fe_3O_4 catalysts with different ratios.

As depicted in Figure 2a,b, the apparent morphology of 4% MoS_2@Fe_3O_4 catalyst was analyzed by scanning electron microscopy (SEM). It can be observed that Fe_3O_4 presented a polyhedral structure with uniform particle size between 50 and 80 nm, and good dispersity. The elemental distribution of MoS_2@Fe_3O_4 was also investigated by EDS element mapping. Figure 2c shows that the O, Fe, Mo, and S elements were uniformly distributed in the surface of sample, which confirmed the successful preparation of MoS_2@Fe_3O_4. Because MoS_2 attached to the Fe_3O_4 surface, the map of Mo and S elements was clearer.

In order to further analyze the microstructure, 4% MoS_2@Fe_3O_4 catalyst was characterized by TEM and HRTEM, and the results are shown in Figure 3. From Figure 3a, it can be seen that the MoS_2 was successfully loaded on the surface of Fe_3O_4 particles, and the MoS_2 had better dispersity and no aggregation phenomenon. At the same time, Fe_3O_4 presented a polyhedral structure with a particle size of about 50–80 nm, which was consistent with the SEM spectra. In Figure 3b, two kinds of lattice fringes can be clearly observed by high-resolution HRTEM. The measured lattice spacing of 0.27 nm corresponded to the (100) crystallographic plane of MoS_2, while that of 0.297 nm corresponded to the (110) crystal plane of Fe_3O_4 [29], which confirmed that MoS_2@Fe_3O_4 catalyst was successfully synthesized.

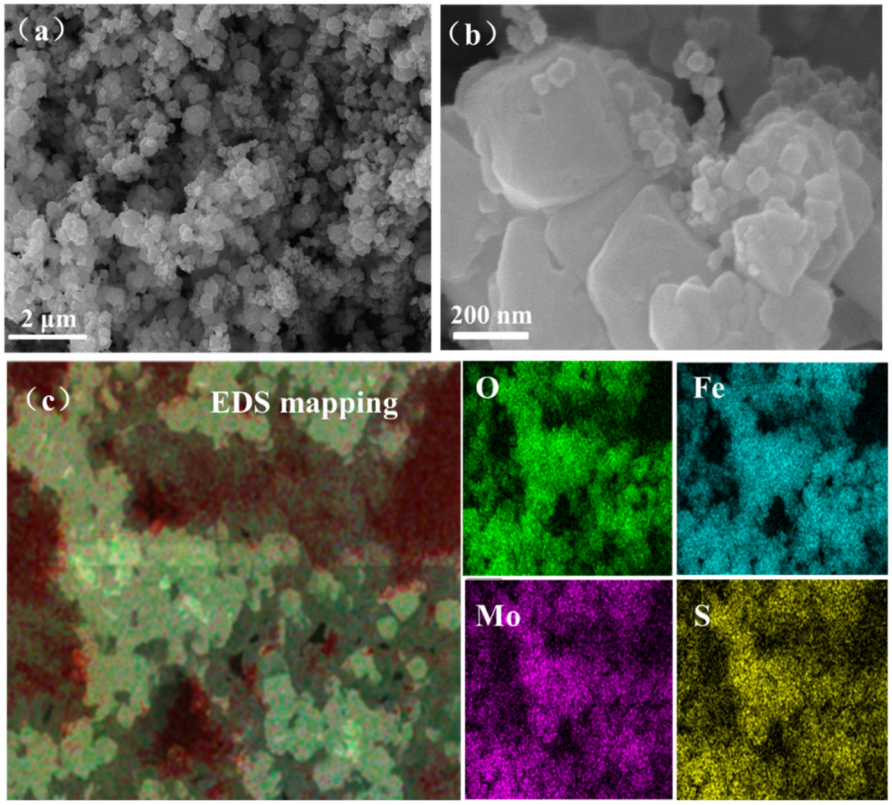


Figure 2. (**a**,**b**) SEM pictures, and (**c**) EDS element mapping of 4% MoS_2@Fe_3O_4 catalyst.

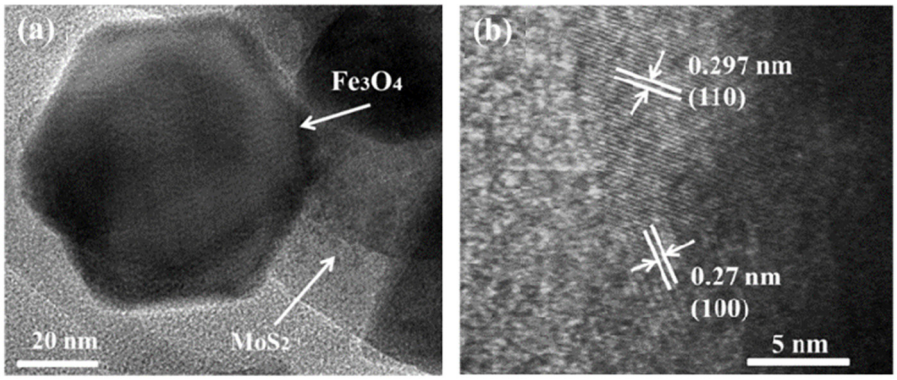


Figure 3. (**a**) TEM and (**b**) HRTEM of 4% MoS_2@Fe_3O_4 catalyst.

An XPS measurement was conducted to reveal the surface elemental composition and chemical state of 4% MoS_2@Fe_3O_4. Figure 4a is the wide scan spectrum of MoS_2@Fe_3O_4 catalyst, indicating the existence of Mo, S, Fe, and O elements on the MoS_2@Fe_3O_4 surface. Meanwhile, the high-resolution XPS spectra of Fe 2p, O 1s, Mo 3d, and S 2p were detected. As shown in Figure 4b, the peaks at 712.64 eV and 726.44 eV were consistent with Fe^{3+} at Fe $2P_{3/4}$ and Fe $2p_{1/2}$, respectively, and the peaks at 709.44 eV and 723.1 eV were fitted with Fe^{2+} at Fe $2P_{3/4}$ and Fe $2p_{1/2}$, respectively [18,30]. The O 1s spectrum in Figure 4c exposed two obvious peaks at 530.3 eV and 531.6 eV, which belonged to Fe−O of Fe_3O_4 and Fe−OH/−OH groups, respectively [31]. The peaks at 232.2 V and 229.3 eV represented Mo $3d_{5/2}$ and Mo $3d_{3/2}$, respectively, which indicated the predominant presence of Mo^{4+} (Figure 4d) [32]. In the S 2p spectrum (Figure 4e), the presence of two peaks at 163.1 eV and 161.8 eV correspond to S $2p_{3/2}$ and S $2p_{1/2}$ stated in metal sulfides [33], respectively.

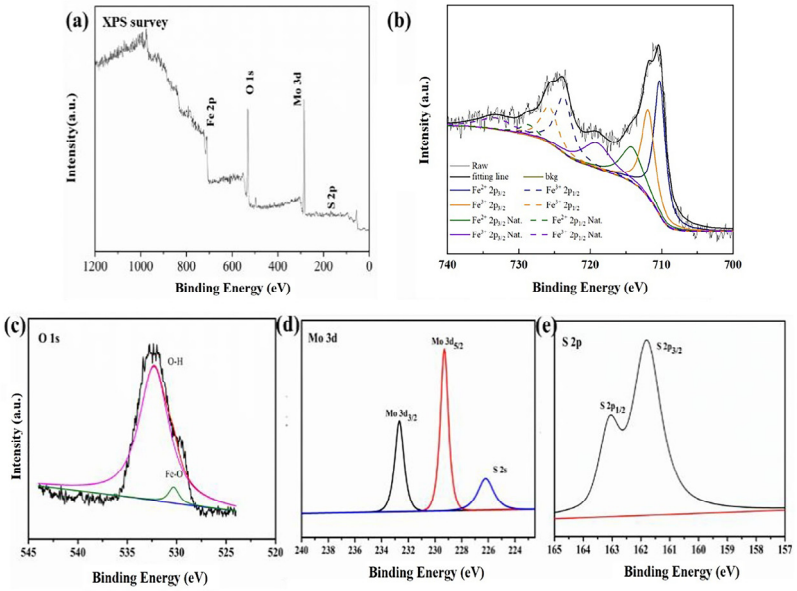


Figure 4. XPS spectra: (**a**) the wide scan, (**b**) Fe 2p, (**c**) O 1s, (**d**) Mo 3d, and (**e**) S 2p of 4% MoS_2@Fe_3O_4 catalyst.

To investigate the electrochemical properties, pure Fe_3O_4, MoS_2, and MoS_2@Fe_3O_4 were tested by AC impedance. As shown in Figure 5, the Nyquist arc radius of 4% MoS_2@Fe_3O_4 was significantly smaller than that of pure Fe_3O_4 and MoS_2 sample, which implied a smaller charge transfer resistance as a result of the fast migration of photogenerated carriers after the introduction of MoS_2 [34]. During the photo-Fenton reaction, the conversion between Fe^{3+} and Fe^{2+} can be promoted, which in turn improved the catalytic activity.

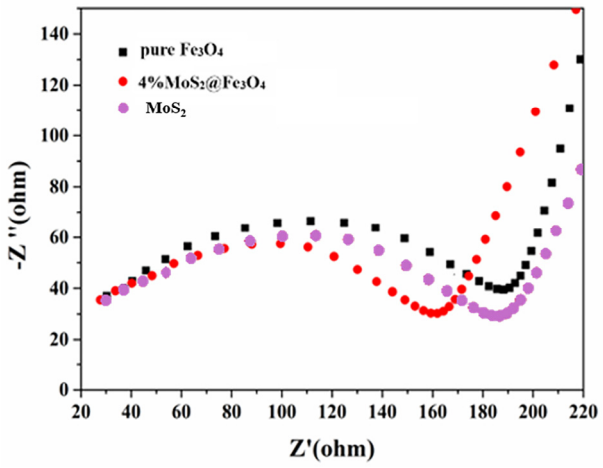


Figure 5. EIS curves of pure Fe_3O_4, MoS_2, and 4% MoS_2@Fe_3O_4 catalyst.

3.2. Evaluation of MoS_2@Fe_3O_4 Photo-Fenton Catalytic Activity

3.2.1. Photo-Fenton Degradation Performance

To evaluate the effect of different mass ratios on the photo-Fenton catalytic performance of MoS_2@Fe_3O_4, three samples were tested under the same reaction conditions: the concentration of TCs was 50 mg/L, solution volume was 200 mL, H_2O_2 concentration was 5 mmol/L, catalyst dosage was 3 g/L, pH was 5.0, and temperature was room temperature. It can be seen from Figure 6a that the TCs degradation efficiency of 2% MoS_2@Fe_3O_4, 4% MoS_2@Fe_3O_4, and 6% MoS_2@Fe_3O_4 materials was 90.8%, 98.6%, and 93.9%, respectively, of which 4% MoS_2@Fe_3O_4 had the best catalytic activity. When the content of MoS_2 was too

small, too high an Fe_3O_4content would hinder the absorption of visible light by MoS_2, so that the quantum yield of light was low and the photocatalytic efficiency was low. When the content of MoS_2 was too large, too low an Fe_3O_4 content would reduce the efficiency of the dominant Fenton reaction. Therefore, 4% MoS_2@Fe_3O_4 had the best photo-Fenton degradation efficiency of TCs, and the latter experiments were chosen 4% MoS_2@Fe_3O_4 as catalyst.

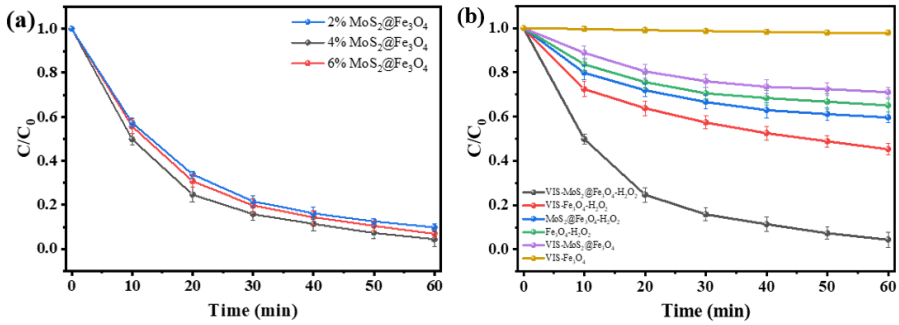


Figure 6. (**a**) The photo-Fenton degradation efficiency of TCs with different mass ratio of MoS_2@Fe_3O_4 and (**b**) Effect of different systems on the degradation of TCs.

To further investigate the catalytic activity of 4% MoS_2@Fe_3O_4, the TCs degradation processes were compared with among different systems, involving vis-Fe_3O_4, Fe_3O_4-H_2O_2, vis-Fe_3O_4-H_2O_2, vis-MoS_2@Fe_3O_4, MoS_2@Fe_3O_4-H_2O_2, and vis-MoS_2@Fe_3O_4-H_2O_2 systems, and the results are shown in Figure 6b (Catalyst = 3 g/L, H_2O_2 = 5 mmol/L, TCs = 50 mg/L, pH = 5, 200 mL). As depicted in Figure 6b, the photocatalytic degradation of TCs was not obvious under visible light irradiation and pure Fe_3O_4 as catalyst. When the MoS_2@Fe_3O_4 catalyst was added, the TCs degradation efficiency during photocatalysis reached 28%. The Fenton system using pure Fe_3O_4 as catalyst exhibited significantly lower TCs degradation efficiency compared to using MoS_2@Fe_3O_4 (39%). Under the condition of photo-Fenton, using MoS_2@Fe_3O_4 as catalyst, the degradation efficiency of TCs reached 98.6%, which was significantly higher than that of pure Fe_3O_4. It indicated that visible light and the Fenton reaction had a synergistic effect, which significantly enhanced the degradation efficiency. Meanwhile, the introduction of MoS_2 can accelerate the Fe^{3+}/Fe^{2+} cycle through electron transfer from Mo^{4+} to Fe^{3+}, resulting in the improvement in degradation efficiency of TCs. At the same time, MoS_2 can enhance the transfer efficiency of photogenerated electron holes and restrain the recombination of electron holes, thus improving the performance of photo-Fenton process. This result was consistent with the previous result of AC impedance.

3.2.2. Different Influencing Factors

The influences of various reaction conditions such as catalyst dosage, H_2O_2 concentration, TCs concentration, initial pH on the photo-Fenton reaction were investigated. The catalytic efficiency of TCs at different catalyst dosage is depicted in Figure 7a (H_2O_2 = 5 mmol/L, TCs = 50 mg/L, pH = 5, 200 mL). The degradation efficiency of TCs increased from 85.1% to 98.6% when the catalyst dosage increased from 1 to 3 g/L, and then reduced to 89.4% with elevated 4% MoS_2@Fe_3O_4 dosage to 5 g/L. The excessive catalyst dosage inhibited the absorption of visible light, reduced the production of photogenerated electrons and holes, and thus lowered the catalytic efficiency. Meanwhile, the scavenging of $OH^{\bullet}$ radicals by excessive Fe^{2+} led to a decline in $OH^{\bullet}$ radical generation [35]. Therefore, the catalyst dosage of 3 g/L was selected in subsequent experiments.

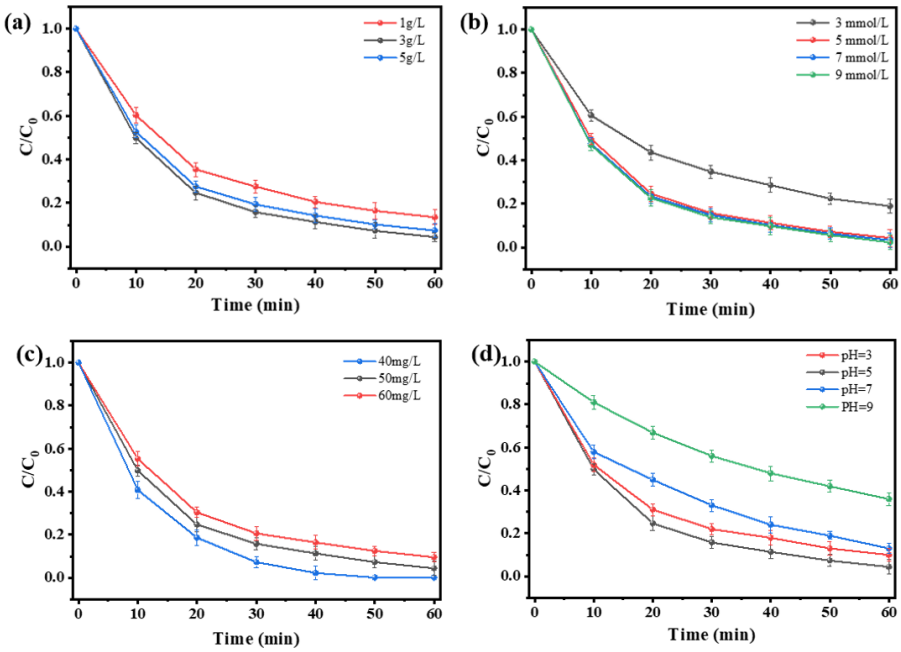


Figure 7. The photo-Fenton degradation efficiency of TCs with (**a**) catalyst dosage, (**b**) H_2O_2 concentrations, (**c**) TCs concentrations, and (**d**) initial pH.

Figure 7b demonstrated that the catalytic efficiency of TCs increased from 82% to 98.6% with the increase in H_2O_2 concentration from 3 mmol/L to 5 mmol/L, and then the efficiency had a slight decline with the further rise in the H_2O_2 concentration to 9 mmol/L (Catalyst = 3 g/L, TCs = 50 mg/L, pH = 5, 200 mL). This might be due to the fact that H_2O_2 was responsible for the formation of $OH^{\bullet}$, and a higher concentration of H_2O_2 would promote to product more $OH^{\bullet}$. However, excessed H_2O_2 may further react with $OH^{\bullet}$ and convert it into $HO_2^{\bullet}$. which was in poor reactivity because of its lower oxidation potential [14]. Therefore, although the H_2O_2 concentration was high, the $OH^{\bullet}$ production decreased, resulting in a lower TCs degradation efficiency. Therefore, 5 mmol/L was selected as the addition concentration of H_2O_2 for subsequent experiments.

The concentration of TCs changed in the range of 40 to 60 mg/L, and the photo-Fenton experiment was carried out (Catalyst = 25 mg, H_2O_2 = 5 mmol/L, pH = 5, 200 mL). As displayed in Figure 7c, the photocatalytic performance of TCs reduced with the increase in TCs concentrations. This was because the amount of catalyst and oxidizer was fixed, so the same number of active species was formed. Meanwhile, high concentrations of TCs may reduce catalyst activity by adsorbing and blocking the surface of the catalyst, or consume H_2O_2 by depleting reactive oxygen species, and trigger side reactions [36]. Considering that the economy, 50 mg/L was determined as the appropriate TCs concentration.

Figure 7d shows the degradation curves of TCs at different pH (Catalyst = 3 g/L, H_2O_2 = 5 mmol/L, TCs = 50 mg/L, 100 mL). The TCs degradation increased from 90% to 98.6% after 60 min with the increase in pH from 3 to 5. According to the pH value of the solution, TCs exists in three forms, specifically, the cationic form when pH < 3.3, the zwitterionic form with a pH of 3.3–7.7, and the anionic form in alkali environment (pH > 7.7) [37]. The cationic form is less vulnerable to reactive oxygen than the zwitterionic form. Consequently, under the condition of pH = 3, TCs cations were formed by protonation, which reduced the degradation efficiency of TCs slightly. When pH further increased to 9 the degradation efficiency of TCs decreased to 62%. This might be due to the quick consumption of H_2O_2 in an alkaline environment. Therefore, pH = 5 was applied in the follow-up experiment.

3.2.3. Stability and Recyclability of MoS_2@Fe_3O_4

In order to evaluate the stability and recyclability of MoS_2@Fe_3O_4 catalyst, the degradation of TCs in recycling experiments was carried out (Catalyst = 3 g/L, H_2O_2 = 5 mmol/L, TCs = 50 mg/L, pH = 5, 200 mL), and the experimental results are displayed in Fig8a. The catalytic efficiency of TCs reduced from 98.6% to 92.1% after five cycles, demonstrating its remarkable stability and reusability. The reason for the slight decrease in degradation efficiency was that the active sites were blocked by the adsorbed TCs and TCs degradation intermediates after repeated use of the catalyst [38]. At the same time, ICP results showed the concentration of the leached iron and molybdenum were 0.021mg/L and 0.009 mg/L, also indicated the MoS_2@Fe_3O_4 catalyst had a better stability. In addition, the MoS_2@Fe_3O_4 catalyst could be easily separated by a magnet after use. To analyze the magnetic characteristics of the samples, hysteresis loop analysis was performed on 4% MoS_2@Fe_3O_4, as shown in Figure 8b. It can be seen that the magnetic saturation value of pure Fe_3O_4 was 63.0 emu/g under an external magnetic field of 10,000 Oe, while that of MoS_2@Fe_3O_4 sample was 43 emu/g, indicating that the magnetism of the catalyst reduced after the introduction of MoS_2. The inset of Figure 8b showed the dispersion of MoS_2@Fe_3O_4 sample in an aqueous solution and in solution after 1 min under an applied magnetic field. MoS_2@Fe_3O_4 sample can be adsorbed by a magnet and the solution became clarified, which indicated that the magnetic properties of the MoS_2@Fe_3O_4 were weaker than those of pure Fe_3O_4, but can still be easily separated and reused under the action of applied magnetic field.

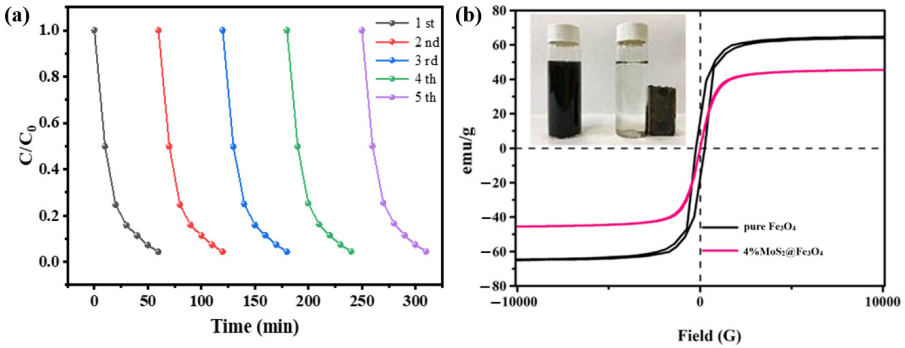


Figure 8. (**a**) Recycling experiments of the degradation system and (**b**) Hysteresis curve of pure Fe_3O_4 and 4% MoS_2@Fe_3O_4 catalyst (the insert represent the collection of 4% MoS_2@Fe_3O_4 by a permanent magnet).

3.3. Degradation Mechanism

In the MoS_2@Fe_3O_4 photo-Fenton system, tertiary-butanol (t-BA), p-benzoquinone (p-BQ), sodium azide (NaN_3) and ammonium oxalate (250 mmol/L) were used as $OH^{\bullet}$, $O_2^{\bullet-}$, $O_2{}^1$ and hole (h+) inhibitors, and dominant active species were evaluated by the quenching experiments. As described in Figure 9a, the order of inhibiting effect on TCs degradation was t-BA > ammonium oxalate > p-BQ > NaN_3. When t-BA was added to the degradation system, the degradation efficiency of TCs dropped nearly to 25.63%, illustrating that $OH^{\bullet}$ was the main free radical, because t-BA is a strong quenching agent of $OH^{\bullet}$. When the degradation of TCs in the quenched h+ system was 72.68%, indicating that photogenerated holes were also the important part of active species in the photo-Fenton system. In contrast, the catalytic efficiency of TCs was hardly affected and was still 90.85% and 96.72% after inhibition of $O_2^{\bullet-}$ and $O_2{}^1$. Therefore, $OH^{\bullet}$ and h+ were the main active groups of TCs degradation in the MoS_2@Fe_3O_4 photo-Fenton system.

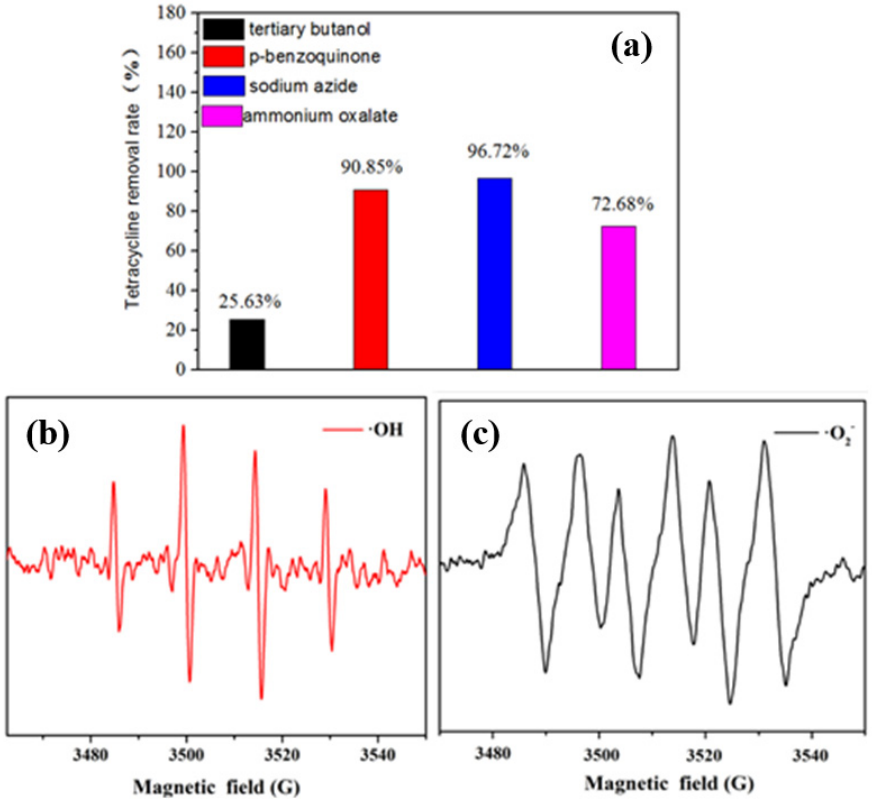


Figure 9. (**a**) Effects of various inhibitors on degradation of TCs, ESR spectra of (**b**) DMPO-OH• and (**c**) DMPO-$O_2^{\bullet-}$ in the MoS_2@Fe_3O_4 photo-Fenton system.

Electron paramagnetic resonance spectroscopy (EPR) trapping tests were used to identify the dominant radical species in in the photo-Fenton system, which further supported the above conclusions. 5,5-dimethyl-1-pyrroline N-oxide (DMPO) was as a radical scavenger of OH• and $O_2^{\bullet-}$ in the MoS_2@Fe_3O_4 photo-Fenton system, and the results are shown in Figure 9b,c. The signal with an intensity ratio of 1:2:2:1 observed under the ultrapure aqueous phase test conditions belonged to the characteristic peak of typical DMPO-OH•, confirming the formation of OH• in the MoS_2@Fe_3O_4 photo-Fenton system (Figure 9b). At the same time, six characteristic peaks with almost equal intensity ratio observed under the methanol phase test conditions belonged to the characteristic peaks of typical DMPO-$O_2^{\bullet-}$, confirming the formation of $O_2^{\bullet-}$ in the MoS_2@Fe_3O_4 photo-Fenton system (Figure 9c). The results of ESR spectra were in good agreement with the quenching experimental results.

4. Conclusions

In this study, a serial of MoS_2@Fe_3O_4 magnetic catalysts were fabricated by a simple hydrothermal process, which had an excellent photo-Fenton catalytic performance. The optimal reaction conditions were evaluated to be the catalyst dosage of 3 g/L, H_2O_2 concentration of 5 mmol/L, initial TCs concentration of 50 mg/L, and pH of 5. The photocatalytic degradation of TCs reached 98.6% within 60 min under the optimal conditions, which was a remarkable growth compared to the pure Fe_3O_4. MoS_2 can accelerate the Fe^{3+}/Fe^{2+} cycle through electron transfer from Mo^{4+} to Fe^{3+}, resulting in the improvement in degradation efficiency of TCs. EPR analysis and free radical quenching experiments results showed that OH• and photogenic hole h+ played a great distribution on TCs degradation. Furthermore, MoS_2@Fe_3O_4 catalytic materials had significant stability and reusability, and can be conveniently collected by a magnet in a real scenario, which would reduce the cost of catalyst separation and recovery.

Author Contributions: Z.-L.L. contributed to overall organizing of all experiments, and writing—original draft preparation. J.-H.S. contributed to gas sensing properties experiments, data analysis. B.L. contributed to sample characterizing and data analysis. Y.-N.C. contributed to sample preparation. W.F. contributed to providing ideas for all the experiments, methodology, and supervision. All authors have read and agreed to the published version of the manuscript.

Funding: This research was funded by the Jilin Science and Technology Development Planning Project [Nos. 20210203006SF, YDZJ202201ZYTS630], the Sixth Batch of Young Science and Technology Talents Promotion Program of Jilin Province [QT202216] and the Educational Department of Jilin Province in China (No. JJKH20210304KJ).

Data Availability Statement: Data are contained within the article.

Acknowledgments: We are grateful to all the authors for their contributions and financial help.

Conflicts of Interest: The authors declare no conflicts of interest.

References

1. Zhang, X.; Xu, B.; Wang, S.; Li, X.; Wang, C.; Liu, B.; Han, F.; Xu, Y.; Yu, P.; Sun, Y. Tetracycline degradation by peroxymonosulfate activated with CoNx active sites: Performance and activation mechanism, Chem. *Eng. J.* **2022**, *431*, 133477. [CrossRef]
2. Wu, Q.; Yang, H.; Kang, L.; Gao, Z.; Ren, F. Fe-based metalorganic frameworks as Fenton-like catalysts for highly efficient degradation of tetracycline hydrochloride over a wide pH range: Acceleration of Fe (II)/Fe (III) cycle under visible light irradiation. *Appl. Catal. B Environ.* **2020**, *263*, 118282. [CrossRef]
3. Zeng, Z.; Ye, S.; Wu, H.; Xiao, R.; Zeng, G.; Liang, J.; Zhang, C.; Yu, J.; Fang, Y.; Song, B. Research on the Sustainable Efficacy of G-MoS_2 Decorated Biochar Nanocomposites for Removing Tetracycline Hydrochloride from Antibiotic-Polluted Aqueous Solution. *Sci. Total Environ.* **2019**, *648*, 206–217. [CrossRef]
4. Wang, M.; Wang, Y.; Li, Y.; Wang, C.; Kuang, S.; Ren, P.; Xie, B. Persulfate oxidation of tetracycline, antibiotic resistant bacteria, and resistance genes activated by Fe doped biochar catalysts: Synergy of radical and non-radical processes. *Chem. Eng. J.* **2023**, *464*, 142558. [CrossRef]
5. Yu, Y.; Jin, Q.; Ren, Y.; Wang, Y.; Zhu, D.; Wang, J. Radiometric fluorescent sensor based on europium (III)-functionalized covalent organic framework for selective and sensitive detection of tetracycline. *Chem. Eng. J.* **2023**, *465*, 142819. [CrossRef]
6. Ji, L.; Chen, W.; Duan, L.; Zhu, D. Mechanisms for strong adsorption of tetracycline to carbon nanotubes: A comparative study using activated carbon and graphite as adsorbents. *Environ. Sci. Technol.* **2009**, *43*, 2322–2327. [CrossRef] [PubMed]
7. Rouhani, M.; Ashrafi, S.D.; Taghavi, K.; Joubani, M.N.; Jaafari, J. Evaluation of tetracycline removal by adsorption method using magnetic iron oxide nanoparticles (Fe_3O_4) and clinoptilolite from aqueous solutions. *J. Mol. Liq.* **2022**, *356*, 119040. [CrossRef]
8. Shan, H.; Si, Y.; Yu, J.; Ding, B. Facile access to highly flexible and mesoporous structured silica fibrous membranes for tetracyclines removal. *Chem. Eng. J.* **2021**, *417*, 129211. [CrossRef]
9. Shao, S.; Hu, Y.; Cheng, J.; Chen, Y. Effects of carbon source, nitrogen source, and natural algal powder-derived carbon source on biodegradation of tetracycline (TEC). *Bioresour. Technol.* **2019**, *288*, 121567. [CrossRef]
10. Wang, Y.; Fan, H.; Keung Wong, P.; Wu, Y.; Rittmann, B. Biodegradation of tetracycline using hybrid material (UCPs-TiO_2) coupled with biofilms under visible light. *Bioresour. Technol.* **2021**, *323*, 124638. [CrossRef] [PubMed]
11. Wang, Y.; Qiang, Z.; Zhu, W.; Yao, W.; Tang, S.; Yang, Z.; Wang, J.; Duan, J.; Ma, C.; Tan, R. $BiPO_4$ nanorod/graphene composite heterojunctions for photocatalytic degradation of tetracycline hydrochloride. *ACS Appl. Nano Mater.* **2021**, *4*, 8680–8689. [CrossRef]
12. Zhi, D.; Wang, J.; Zhou, Y.; Luo, Z.; Sun, Y.; Wan, Z.; Luo, L.; Tsang, D.C.W.; Dionysiou, D.D. Development of ozonation and reactive electrochemical membrane coupled process: Enhanced tetracycline mineralization and toxicity reduction. *Chem. Eng. J.* **2020**, *383*, 123149. [CrossRef]
13. Li, X.; Cui, K.; Guo, Z.; Yang, T.; Cao, Y.; Xiang, Y.; Chen, H.; Xi, M. Heterogeneous Fenton-like degradation of tetracyclines using porous magnetic chitosan microspheres as an efficient catalyst compared with two preparation methods. *Chem. Eng. J.* **2020**, *379*, 122324. [CrossRef]
14. Nie, M.; Li, Y.; He, J.; Xie, C.; Wu, Z.; Sun, B.; Zhang, K.; Kong, L.; Liu, J. Degradation of tetracycline in water using Fe_3O_4 nanospheres as Fenton-like catalysts: Kinetics, mechanisms and pathways. *New J. Chem.* **2020**, *44*, 2847–2857. [CrossRef]
15. Qin, G.; Song, X.; Chen, Q.; He, W.; Yang, J.; Li, Y.; Zhang, Y.; Wang, J.; Dionysiou, D.D. Novel durable and recyclable Cu@MoS_2/polyacrylamide/copper alginate hydrogel photo-Fenton-like catalyst with enhanced and self-regenerable adsorption and degradation of high concentration tetracycline. *Appl. Catal. B Environ. Energy* **2024**, *344*, 123640. [CrossRef]
16. Lai, C.; Shi, X.; Li, L.; Cheng, M.; Liu, X.; Liu, S.; Li, B.; Yi, H.; Qin, L.; Zhang, M.; et al. Enhancing iron redox cycling for promoting heterogeneous Fenton performance: A review. *Sci. Total Environ.* **2021**, *775*, 145850. [CrossRef] [PubMed]

17. Ju, J.H.; Chen, Y.T.; Liu, Z.Q.; Huang, C.; Li, Y.Q.; Kong, D.Z.; Shen, W.; Tang, S. Modification and application of Fe_3O_4 nanozymes in analytical chemistry: A review. *Chin. Chem. Lett.* **2023**, *34*, 107820. [CrossRef]
18. Dhiman, P.; Sharma, J.; Kumar, A.; Sharma, G.; Dawi, E.A. Photocatalytic degradation of malachite green by waste derived bio-char impregnated Bi_5O_7Br/Fe_3O_4 magnetic composite. *Opt. Materials.* **2023**, *146*, 114568. [CrossRef]
19. Liu, Q.; Zhou, L.; Liu, L.; Li, J.; Wang, S.; Znad, H.; Liu, S. Magnetic ZnO @ Fe_3O_4 Composite for self-generated H_2O_2 toward photo-Fenton-l'ike oxidation of nitrophenol. *Compos. Part B* **2020**, *200*, 108345. [CrossRef]
20. Wang, Z.; Mi, B. Environmental applications of 2D molybdenum disulfide (MoS_2) nanosheets. *Environ. Sci. Technol.* **2017**, *51*, 8229–8244. [CrossRef]
21. Li, T.; Yin, W.; Zhang, P.; Zhao, X.; Wei, R.; Zhou, W.; Tu, X. Dual heterojunctions and sulfur vacancies of $AgInS_2/rGO/MoS_2$ co-induced photocatalytic degradation of tetracycline hydrochloride. *Colloids Surf. A Physicochem. Eng. Asp.* **2023**, *667*, 131396. [CrossRef]
22. Peng, J.; Weng, J. Enhanced peroxidase-like activity of MoS_2/graphene oxide hybrid with light irradiation for glucose detection. *Biosens. Bioelectron.* **2017**, *89*, 652–658. [CrossRef] [PubMed]
23. Dou, X.N.; Zhang, Q.; Shah, S.N.A.; Khan, M.; Uchiyama, K.; Lin, J.M. MoS_2-quantum dot triggered reactive oxygen species generation and depletion: Responsible for enhanced chemiluminescence. *Chem. Sci.* **2019**, *10*, 497–500. [CrossRef] [PubMed]
24. Hu, S.Y.; Li, Y.Y.; Zang, C.J.; Ma, X.J.; Zhao, B.; Chen, F. Piezoelectric field-promoted heterogeneous sono-Fenton performance of MoS_2/α-Fe_2O_3 heterojunction structure. *Appl. Surf. Sci.* **2020**, *534*, 147499. [CrossRef]
25. Luo, H.W.; Cheng, Y.; Zeng, Y.F.; Luo, K.; Pan, X.L. Enhanced decomposition of H_2O_2 by molybdenum disulfide in a Fenton-like process for abatement of organic micropollutants. *Sci. Total Environ.* **2020**, *732*, 139335. [CrossRef]
26. Chang, Q.; Zhu, L.; Yu, C.; Tang, H.; He, Q.T. Synthesis and properties of magnetic and luminescent Fe_3O_4/SiO_2/Dye/SiO_2 nanoparticles. *J. Luminescent.* **2008**, *128*, 1890–1895. [CrossRef]
27. Jiang, H.; Sun, Y.; Feng, J.; Wang, J. Heterogeneous electro-Fenton oxidation of azo dye methyl orange catalyzed by magnetic Fe_3O_4 nanoparticles. *Water Sci. Technol.* **2016**, *74*, 1116–1126. [CrossRef] [PubMed]
28. Dhiman, V.; Kondal, N.; Prashant; Dhiman, P.; Kumari, A.; Sharma, R. Bryophyllum Pinnatum leaf extract mediated MoS_2/ZnO nanocomposite for robust photocatalysis applications. *J. Mol. Struct.* **2024**, *1318*, 139196. [CrossRef]
29. Li, G.; Gu, B.; Luo, Y.; Fan, G.; Yu, X. Architecture engineering of Fe/Fe_2O_3@MoS_2 enables highly efficient tetracycline remediation via peroxymonosulfate activation: Critical roles of adsorption capacity and redox cycle regulation. *J. Environ. Manag.* **2024**, *353*, 120210. [CrossRef]
30. Gao, Z.; Wu, H.; Liu, Z.; Liu, L.; Zeng, Z.; Yang, X.; Wang, H.; Du, J.; Zheng, B.; Guo, Y. Composites of Fe_3O_4, Ag, and Au Nanoparticles for Dye Degradation and Selective Detection of Glutathione. *ACS Appl. Nano Mater.* **2023**, *6*, 11531–11540. [CrossRef]
31. Han, T.; Wei, Y.; Jin, X.; Jiu, H.; Zhang, L.; Sun, Y.; Tian, J.; Shang, R.; Hang, D.; Zhao, R. Hydrothermal self-assembly of α-Fe_2O_3 nanorings@ graphene aerogel composites for enhanced Li storage performance. *J. Mater. Sci.* **2019**, *54*, 7119–7130. [CrossRef]
32. Li, X.T.; Lv, X.D.; Li, N.; Wu, J.J.; Zheng, Y.Z.; Tao, X. One-step hydrothermal synthesis of high-percentage 1T-phase MoS_2 quantum dots for remarkably enhanced visible light-driven photocatalytic H_2 evolution. *Appl. Catal. B Environ.* **2019**, *243*, 76–85. [CrossRef]
33. Zhou, Q.; Yao, Z.; Wang, H.; Yang, J.; Zhang, Y.; Qian, L.; Zhang, S. Interface engineering of NixSy@MoS_2 heterostructure nanorods as high-efficient electrocatalysts for water splitting. *Int. J. Hydrogen Energy* **2021**, *46*, 35077–35087. [CrossRef]
34. Narewadikar, N.A.; Pedanekar, R.S.; Parale, V.G.; Park, H.H.; Rajpure, K.Y. Spray deposited yttrium incorporated TiO_2 photoelectrode for efficient photo electrocatalytic degradation of organic pollutants. *J. Rare Earths* **2023**, *41*, 1929–1937. [CrossRef]
35. Scaria, J.; Nidheesh, P.V. Magnetite−reduced graphene oxide nanocomposite as an efficient heterogeneous Fenton catalyst for the degradation of tetracycline antibiotics. *Environ. Sci. Water Res. Technol.* **2022**, *8*, 1261–1276. [CrossRef]
36. Zhao, Y.; Cao, Z.; Chen, Y.; Jia, Y.; Wang, Q.; Cheng, H. Heterostructure coal-bearing strata kaolinite/$MnFe_2O_4$ composite for activation of peroxydisulfate to efficiently degrade chlortetracycline hydrochloride. Colloids Surf. *A Physicochem. Eng. Asp.* **2022**, *643*, 128789. [CrossRef]
37. Chang, P.-H.; Li, Z.; Jiang, W.-T.; Jean, J.-S. Adsorption and intercalation of tetracycline by swelling clay minerals. *Appl. Clay Sci.* **2009**, *46*, 27–36. [CrossRef]
38. Yang, X.; He, J.; Yang, Q.; Jiao, R.; Liao, G.; Wang, D. Cu(I)-doped Fe_3O_4 nanoparticles/porous composite for enhanced H_2O_2 oxidation of carbamazepine. *J. Colloid Interface Sci.* **2019**, *551*, 16–25. [CrossRef]

Disclaimer/Publisher's Note: The statements, opinions and data contained in all publications are solely those of the individual author(s) and contributor(s) and not of MDPI and/or the editor(s). MDPI and/or the editor(s) disclaim responsibility for any injury to people or property resulting from any ideas, methods, instructions or products referred to in the content.